High-Resolution MIMO Millimeter-Wave Radar Imaging Method for Non-Cooperative Targets

Guan Jixing *, An Junyu, Liao Guisheng

Posted Date: 27 March 2026

doi: 10.20944/preprints202603.2203.v1

Keywords: MIMO millimeter-wave imaging radar; array errors; super-resolution; BP imaging; concealed object detection

 doi:10.20944/preprints202603.2203.v1

Article

High-Resolution MIMO Millimeter-Wave Radar Imaging Method for Non-Cooperative Targets

Guan Jixing [1,*], An Junyu [2] and Liao Guisheng [1]

[1] National Key Laboratory of Radar Signal Processing, Xidian University

[2] Information Science Academy, China Electronics Technology Group Corporation

* Correspondence: guanjixing1979@sohu.com

Abstract

In the field of security screening imaging, millimeter-wave technology offers high imaging resolution and low radiation energy. However, it faces challenges such as difficulty in imaging non-cooperative moving targets, as well as bulky equipment and high costs. This paper proposes a high-resolution imaging method based on MIMO millimeter-wave radar. Firstly, the array model and slant range model are established, and a two-dimensional resolution scheme in range and height is constructed using a one-dimensional MIMO linear array and wideband signals. Then, the algorithm flow for MIMO millimeter-wave radar imaging is designed, and a range-domain super-resolution algorithm is introduced. This paper compensates for the phase coupling introduced by the transmitting array and target motion, and successfully achieves two-dimensional imaging of non-cooperative targets based on the back-projection principle. Subsequently, the influence of array errors on the imaging results is analyzed. This method compensates for the phase coupling introduced by the transmit array and target motion, and provides theoretical analysis of array arrangement errors. E Finally, the experimental results of the MIMO radar are analyzed. The final measured processing results show that the system can clearly reveal metal objects through cloth occlusion, and super-resolution processing yields sharper contours in the imaging of metal plates. Simulation analysis of imaging with array errors indicates that among the azimuth–elevation–range array position errors, the range array position error has a relatively significant impact.

Keywords: MIMO millimeter-wave imaging radar; array errors; super-resolution; BP imaging; concealed object detection

1. Introduction

In the face of the current complex public security environment worldwide, particularly in high-density pedestrian areas such as aviation hubs and rail transit stations, traditional security screening methods are confronted with significant challenges. Therefore, an imaging technology capable of efficiently screening concealed items carried on the human body, with non-invasive, non-stop, and covert characteristics, has become an urgent demand in the security field [1–4]. Although X-ray technology possesses imaging capability, X-ray-based detection methods are unsuitable for detecting concealed items on the human body due to excessive ionizing radiation, and they also raise privacy concerns. X-ray methods are primarily used for luggage screening [5–7]. Consequently, millimeter-wave and terahertz imaging technologies, owing to their high resolution, non-ionizing radiation, and ability to penetrate clothing, have been applied in imaging detection [8–10].

In millimeter-wave near-field imaging, achieving sufficient signal-to-noise ratio within a limited observation time imposes extremely high requirements on the spatial scanning speed. Traditional mechanical scanning systems, constrained by physical inertia, suffer from low data refresh rates, are prone to imaging blur for dynamic targets, and thus fail to meet real-time imaging requirements [8,11,12]. In contrast, electronic scanning technology, with its microsecond-level beam switching speed, has become the ideal choice for achieving rapid echo accumulation. The two-dimensional

 doi:10.20944/preprints202603.2203.v1

multiple-input multiple-output (MIMO) millimeter-wave radar developed by Rohde & Schwarz (e.g., the QPS series) eliminates mechanical moving components. It innovatively employs a planar sparse array combined with time-division multiplexing (TDM) orthogonal waveform technology, successfully addressing the issues of imaging speed and resolution, and achieving high-precision three-dimensional real-time imaging. The three-dimensional security screening imaging results are shown in Figure 1 [13]. However, due to the large number of channels required by the two-dimensional array configuration, the equipment cost is high. Furthermore, completing full-aperture TDM transmission requires a long cycle, which extends the effective accumulation time of the system. Additionally, in practical hardware systems, position errors of the array antenna elements are unavoidable. If these non-ideal factors are not properly analyzed and calibrated, they will lead to defocusing of imaging results and elevated sidelobe levels, thereby severely constraining the high-resolution imaging performance of the system [14–16]. Moreover, limited by the physical aperture size, the resolution of conventional algorithms is inherently constrained by the Rayleigh limit. It is difficult to break through the physical resolution bottleneck merely by increasing algorithm complexity, and this is often accompanied by high sidelobe levels, which are unfavorable for fine imaging of densely concealed objects.

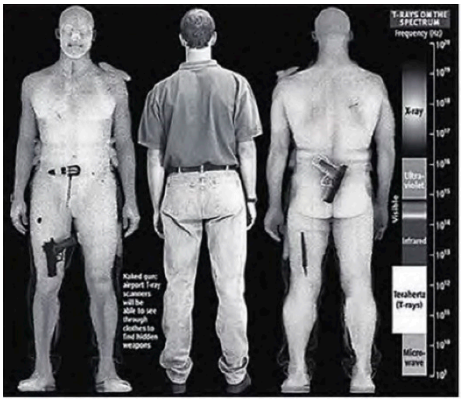

Figure 1. Three-dimensional security screening system image.

To address the limitations of existing imaging technologies, this paper proposes a high-resolution imaging method for non-cooperative target MIMO millimeter-wave radar. In the system architecture, an accurate array-target near-field slant range model is established. By leveraging wideband millimeter-wave signals and the virtual aperture synthesis technique of a MIMO linear array, the number of physical array elements is significantly reduced while achieving high-precision projection imaging in the range-elevation two-dimensional plane. Meanwhile, considering non-ideal factors in practical systems, an array error model is established, and the impact of array errors on imaging quality is analyzed. In the signal processing part, Doppler-domain compensation and Back-Projection (BP) algorithms are employed to achieve target focusing [17–20]. To further overcome the resolution limitation imposed by the physical aperture of the array, a super-resolution processing algorithm is introduced [21,22]. In the experimental part, tests are conducted on a metal plate wrapped in a fabric bag and on a moving scenario where a human body carries the concealed object. These tests confirm the radar system's ability to detect metal objects through fabric obstruction and the improvement in imaging performance by super-resolution processing. Finally, simulation experiments are performed to analyze the impact of array errors on imaging.

 doi:10.20944/preprints202603.2203.v1

2. MIMO Radar Array and Imaging Geometry Model

2.1. Array Model

The structure of the transmit-receive linear array in this paper is shown in Figure 2. To describe the spatial positions of the array elements, a Cartesian coordinate system is established as follows: the antenna linear array is located in the XOZ plane, where the X-axis is defined as the azimuth direction, the Z-axis is defined as the elevation direction, and the Y-axis perpendicular to the array plane is defined as the range direction. The receiving elements are centrally arranged in the middle of the array, while the transmitting elements are divided into two groups symmetrically placed on both sides of the receiving array along the Z-axis. The transmit and receive arrays are not aligned in the X-direction [23]. Based on the above coordinate system, the mathematical models of the transmit and receive arrays can be expressed as (x_t, y_t, z_t) and (x_r, y_r, z_r), with the spacing between the transmit and receive arrays denoted as d_{tr}. The number of transmit array elements is set as N_{tx} and N_{tz}, with spacings d_{tx} and d_{tz} in the X and Z directions, respectively. The number of receive array elements is N_{rx} and N_{rz}, with spacings d_{rx} and d_{rz} in the X and Z directions, respectively. In this paper, the array arrangement satisfies the following relationships:

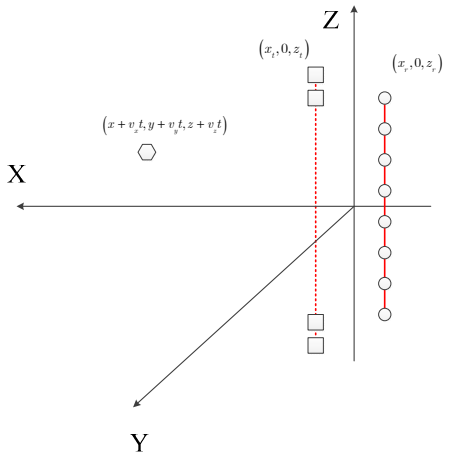

Figure 2. XOZ coordinate system array distribution model.

$$\begin{cases} x_t = -\dfrac{d_{tr}}{2} \\ y_t = 0 \\ z_t = \left[-\dfrac{(N_{rz}-1)d_{rz}}{2} + \left(-\dfrac{N_{tz}}{2}:-1\right)d_{tz}, \dfrac{(N_{rz}-1)d_{rz}}{2} + \left(0:\dfrac{N_{tz}}{2}-1\right)d_{tz}\right] \\ x_r = d_{tr}/2 \\ y_r = 0 \\ z_r = \left[-\dfrac{(N_{rz}-1)}{2}:\dfrac{(N_{rz}-1)}{2}\right]d_{rz} \end{cases} \quad (1)$$

The spacing between the transmitter and receiver satisfies $d_{rz} = N_{tz}d_{tz}/2$. Accordingly, Eq. (1) can be further expressed as:

 doi:10.20944/preprints202603.2203.v1

$$\begin{cases} x_t = -\dfrac{d_{tr}}{2} \\ z_t = \left[-\dfrac{(N_{rz}-1)N_{tz}}{4} + \left(-\dfrac{N_{tz}}{2}:-1\right), \dfrac{(N_{rz}-1)N_{tz}}{4} + \left(0:\dfrac{N_{tz}}{2}-1\right)\right] d_{tz} \\ x_r = \dfrac{d_{tr}}{2} \\ z_r = \dfrac{\left[-\dfrac{(N_{rz}-1)}{2}:\dfrac{(N_{rz}-1)}{2}\right] N_{tz} d_{tz}}{2} \end{cases} \tag{2}$$

Then, the following constraints are satisfied:

$$\begin{aligned} \left[-\frac{(N_{rz}+1)N_{tz}}{4}\right] d_{tz} \le z_t \le \left[\frac{(N_{rz}+1)N_{tz}}{4} - 1\right] d_{tz} \\ -\frac{(N_{rz}-1)N_{tz}d_{tz}}{4} \le z_r \le \frac{(N_{rz}-1)N_{tz}d_{tz}}{4} \\ \left(-\frac{N_{rz}N_{tz}}{2}\right) d_{tz} \le z_t + z_r \le \left(\frac{N_{rz}N_{tz}}{2} - 1\right) d_{tz} \\ -\frac{(N_{rz}N_{tz}+N_{tz})}{2d_{tz}} \le z_t - z_r \le \frac{(2N_{rz}N_{tz}+2N_{tz}-1)}{4d_{tz}} \end{aligned} \tag{3}$$

The Z-direction size of the receive sub-array D_z and the Z-direction size of the transmit sub-array D_z can be expressed as:

$$D_{rz} = \frac{N_{rz}N_{tz}d_{tz}}{2}, D_{tz} = \frac{N_{tz}d_{tz}}{2} \tag{4}$$

then the following conditions are satisfied:

$$\begin{aligned} -\frac{D_{rz}+D_{tz}}{2} \le z_t \le \frac{[D_{rz}+D_{tz}-2d_{tz}]}{2} \\ -\frac{D_{rz}-D_{tz}}{2} \le z_t \le \frac{D_{rz}-D_{tz}}{2} \\ -D_{rz} \le z_r + z_t \le D_{rz} - d_{tz} \\ z_t^2 + z_r^2 \le \frac{D_{rz}^2 + D_{tz}^2}{2} \\ -(D_{rz}+D_{tz}) \le z_t - z_r \le D_{rz} + D_{tz} - \frac{1}{4d_{tz}} \end{aligned} \tag{5}$$

2.2. Slant Range Model

Based on the array model in Section 2.1, the radar received signal slant range model is established. The MIMO radar has a total of M transmitting elements that transmit sequentially in TDM mode, and N receiving elements receive signals simultaneously. The signal duration for each transmit element is T_r, and a coherent processing interval contains I complete transmission periods. Therefore, the total coherent integration time of the system can be expressed as $T_i = IMT_r$. The continuous time t can be expressed as the sum of three terms: the fast time t_r, the time for one transmission period t_m, and the slow time t_i:

$$t = t_r + t_m + t_i = t_r + mT_r + iMT_r \tag{6}$$

where $m\,(m = 0, 1, \ldots, M-1)$ denotes the m-th transmit element, and $i\,(i = 0, 1, 2, \ldots, I-1)$ denotes the i-th transmission period.

The target coordinates are (x, y, z) and the velocity can be expressed as (v_x, v_y, v_z). Then the slant range can be expressed as:

 doi:10.20944/preprints202603.2203.v1

$$R = \frac{1}{2}\left[\begin{array}{l}\sqrt{(x+v_x t-x_t)^2+\left(y+v_y t-y_t\right)^2+(z+v_z t-z_t)^2} \\ +\sqrt{(x+v_x t-x_r)^2+\left(y+v_y t-y_r\right)^2+(z+v_z t-z_r)^2}\end{array}\right] \approx R_{tr}+vt \tag{7}$$

$$\begin{aligned} R_{tr} &= \frac{1}{2}\left[\sqrt{(x-x_t)^2+(y-y_t)^2+(z-z_t)^2}+\sqrt{(x-x_r)^2+(y-y_r)^2+(z-z_r)^2}\right] \\ v &= \frac{1}{2}\left[\frac{(x-x_t)v_x+(y-y_t)v_y+(z-z_t)v_z}{\sqrt{(x-x_t)^2+(y-y_t)^2+(z-z_t)^2}}+\frac{(x-x_r)v_x+(y-y_r)v_y+(z-z_r)v_z}{\sqrt{(x-x_r)^2+(y-y_r)^2+(z-z_r)^2}}\right] \end{aligned} \tag{8}$$

where R_{tr} and v denote the initial slant range and the equivalent velocity of the target, respectively. Under this condition, the echo signal delay caused by target motion is expressed as:

$$\tau(t_r, t_i, m, n) \approx \frac{2}{c}R = \frac{2}{c}\left[R_{tr}+v(t_r+t_m+t_i)\right] \tag{9}$$

The slant range R_{tr}between the target and the transmit-receive array can be further expressed as

$$\begin{aligned} R_{tr} \approx\ & R_0 - \frac{1}{2}\left[\sin\theta_x(x_t+x_r)+\sin\theta_y(y_t+y_r)+\sin\theta_z(z_t+z_r)\right] \\ & + \frac{1}{4R_0}\left[\begin{array}{l}\cos^2\theta_x({x_t}^2+{x_r}^2)+\cos^2\theta_y({y_t}^2+{y_r}^2)+\cos^2\theta_z({z_t}^2+{z_r}^2) \\ -2\sin\theta_x\sin\theta_z(x_t z_t+x_r z_r) \\ \ -2\sin\theta_y\sin\theta_z(y_t z_t+y_r z_r)-2\sin\theta_x\sin\theta_y(x_t y_t+x_r y_r)\end{array}\right] \\ & + \frac{1}{4{R_0}^2}\left\{\begin{array}{l}\sin\theta_x\cos^2\theta_x(x_t^3+x_r^3)+\sin\theta_y\cos^2\theta_y(y_t^3+y_r^3) \\ +\sin\theta_z\cos^2\theta_z(z_t^3+z_r^3) \\ +(1-3\sin^2\theta_z)\left[\sin\theta_x(x_t z_t^2+x_r z_r^2)+\sin\theta_y(y_t z_t^2+y_r z_r^2)\right] \\ +(1-3\sin^2\theta_x)\left[\sin\theta_y(x_t^2 y_t+x_r^2 y_r)+\sin\theta_z(x_t^2 z_t^2+x_r^2 z_r)\right] \\ +\left(1-3\sin^2\theta_y\right)\left[\sin\theta_x(x_t y_t^2+x_r y_r^2)+\sin\theta_z(y_t^2 z_t^2+y_r^2 z_r)\right] \\ -6\sin\theta_x\sin\theta_y\sin\theta_z(x_t y_t z_t+x_r y_r z_r)\end{array}\right\} \end{aligned} \tag{10}$$

Taking the geometric center of the antenna array as the observation point, $R_0 = \sqrt{x^2+y^2+z^2}$is defined as the slant range to the target, and θ_x, θ_y, and $\theta_z$are angles describing the spatial direction of the target, which can be expressed as $\sin\theta_x = \frac{x}{R_0}$, $\sin\theta_y = \frac{y}{R_0}$, $\sin\theta_z = \frac{z}{R_0}$.

2.3. Imaging Geometry Model and MIMO Radar Parameter Design

The system performs imaging in the YZ plane, using the signal bandwidth and array aperture to achieve range (Y) and elevation (Z) resolution, respectively. As shown in Figure 3, to obtain range-elevation imaging, the system employs squint imaging. The radar line of sight has a fixed squint angle with the target in the XY plane. By setting the squint observation angle, the target width feature is geometrically projected onto the range dimension. In principle, this is similar to the synthetic aperture radar (SAR) technique that projects the three-dimensional ground surface onto a two-dimensional plane.

The MIMO millimeter-wave radar has a height of 1.2 m and a center frequency of 95 GHz. The system employs a 10 GHz bandwidth signal, ensuring a range resolution of 0.02 m under a range broadening factor of 1.2. The equivalent aperture size in the elevation direction must be no less than 1.26 m, to ensure an elevation resolution of 0.015 m under an elevation broadening factor of 1.2. To optimize sidelobe performance, an 8Tx/16Rx MIMO architecture is adopted, with a Tx spacing of 1.1 cm and an Rx spacing of 4.4 cm. Through virtual aperture synthesis, 128 equivalent elements are obtained, with a total equivalent physical aperture of 1.4 m [4]. The imaging distance from the radar to the target is 5 m, and the imaging area size is 0.5 m.

 doi:10.20944/preprints202603.2203.v1

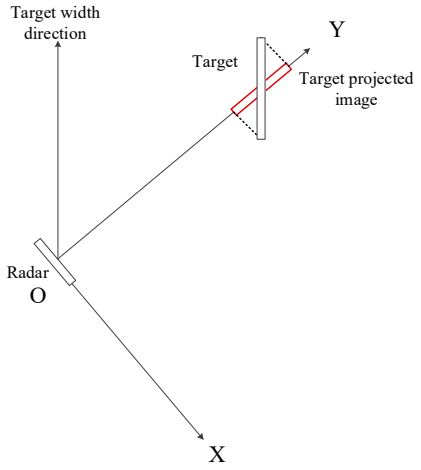

Figure 3. Imaging geometric relationship.

3. Signal Processing Algorithm

The MIMO millimeter-wave radar imaging algorithm flow is shown in Figure 4, with specific implementation detailed in Ref. [4]. In the MIMO millimeter-wave radar imaging algorithm flow, range-domain FFT is performed to achieve range focusing. However, the resolution of FFT is physically limited. If the spacing between two targets is smaller than the range resolution, a broad peak will form in the FFT spectrum, and the radar cannot distinguish the two targets. Therefore, when the signal bandwidth is limited, super-resolution methods are needed to improve the range resolution. This paper adopts the Iterative Adaptive Approach (IAA). IAA is an adaptive iterative algorithm based on weighted least squares, which performs spectral estimation using weighted least squares as the cost function. It constructs the signal covariance matrix from the spectral estimation results of the previous iteration, and uses its inverse as the weighting matrix in the weighted least squares solution. IAA does not require prior knowledge of the number of signal sources. It can achieve super-resolution effectively with only a few or even a single snapshot. In the imaging flow described above, the range FFT is replaced by IAA super-resolution. The range-domain data for all receive channels and all accumulated pulses in the three-dimensional range-accumulation-receive channel data are processed with IAA. The range-domain data is defined as $\boldsymbol{x} \in \mathbb{C}^{N_s \times 1}$, where N_s is the number of range points. The range scanning steering matrix is defined as: $\boldsymbol{A}(R) = [\boldsymbol{a}(R_1), \boldsymbol{a}(R_2), \cdots, \boldsymbol{a}(R_l), \cdots, \boldsymbol{a}(R_L)], l = 1, \cdots, L$, $\boldsymbol{a}(R_l) = \left[1, e^{j2\pi K_r 2R_l/(cf_s)}, \cdots, e^{j2\pi K_r (N_s-1)2R_l/(cf_s)}\right]^T$, where L is the total number of scanning grid points and f_s is the sampling rate. K_r is the chirp rate.

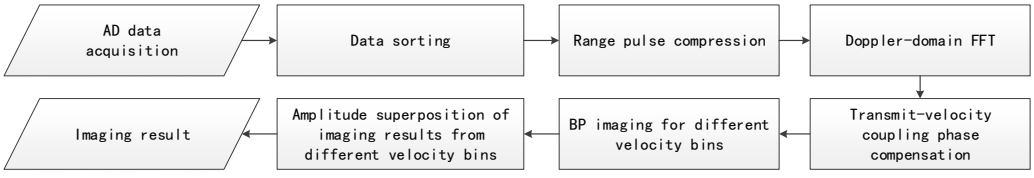

Figure 4. MIMO millimeter-wave radar imaging algorithm flow.

The algorithm procedure is as follows:

Initialization: Calculate the initial complex amplitude for the *l*-th scanning range according to:

 doi:10.20944/preprints202603.2203.v1

$\alpha_l^{(0)} = \frac{\boldsymbol{a}^{\mathrm{H}}(R_l)\boldsymbol{x}}{\boldsymbol{a}^{\mathrm{H}}(R_l)\boldsymbol{a}(R_l)}$ to obtain L initial power vector elements $\boldsymbol{p}^{(0)} = \left[\left|\alpha_1^{(0)}\right|^2, \left|\alpha_2^{(0)}\right|^2, \cdots, \left|\alpha_l^{(0)}\right|^2, \cdots, \left|\alpha_L^{(0)}\right|^2\right]^{\mathrm{T}}$.

Iteration: Compute the covariance matrix for the q-th ($q \le Q$, where Q is the maximum number of iterations) iteration $\boldsymbol{R}^q = \boldsymbol{A}(R)diag\left(\boldsymbol{p}^{(q-1)}\right)\boldsymbol{A}^{\mathrm{H}}(R)$.Compute the complex amplitude for the l -th scanning range $\alpha_l^{(q)} = \frac{\boldsymbol{a}^{\mathrm{H}}(R_l)(\boldsymbol{R}^q)^{-1}\boldsymbol{x}}{\boldsymbol{a}^{\mathrm{H}}(R_l)(\boldsymbol{R}^q)^{-1}\boldsymbol{a}(R_l)}$, to obtain the initial power vector $\boldsymbol{p}^{(q)} = \left[\left|\alpha_1^{(q)}\right|^2, \left|\alpha_2^{(q)}\right|^2, \cdots, \left|\alpha_l^{(q)}\right|^2, \cdots, \left|\alpha_L^{(q)}\right|^2\right]^{\mathrm{T}}$. Iterate until the power vector converges or the maximum number of iterations is reached. The complex amplitude values for all scanning ranges from the last iteration are obtained. Subsequently, Doppler-domain FFT and other imaging processes are performed.

4. Array Error Analysis

In this paper, the ideal array arrangement satisfies Eq. (1), but in practice, deviations from Eq. (1) exist due to errors. For Eq. (10), under ideal conditions where $y_{t0} = y_{r0} = 0, x_{t0} + x_{r0} = 0$, the expression can be simplified as:

$$\begin{aligned} R_{tr_0} \approx\ & R_0 - \frac{1}{2}\left[\sin\theta_z\left(z_{t0} + z_{r_0}\right)\right] \\ & + \frac{1}{4R_0}\left[\cos^2\theta_x\left(x_{t0}^2 + x_{r_0}^2\right) + \cos^2\theta_z\left(z_{t0}^2 + z_{r_0}^2\right) - 2\sin\theta_x\sin\theta_z\left(x_{t0}z_{t0} + x_{r_0}z_{r_0}\right)\right] \\ & + \frac{1}{4R_0^2}\left\{\begin{array}{l}\sin\theta_x\cos^2\theta_x\left(x_{t0}^3 + x_{r_0}^3\right) + \sin\theta_z\cos^2\theta_z\left(z_{t0}^3 + z_{r_0}^3\right) \\ +(1 - 3\sin^2\theta_x)\sin\theta_x\left(x_{t0}^2 z_{t0} + x_{r_0}^2 z_{r_0}\right) + (1 - 3\sin^2\theta_z)\sin\theta_z\left(x_{t0}^2 z_{t0} + x_{r_0}^2 z_{r_0}\right)\end{array}\right\} \end{aligned} \tag{11}$$

The signal after MTD and phase compensation is:

$$\begin{aligned} s(f_r, f_i, m, n) = \exp\left(-\mathrm{j}\frac{4\pi f_o}{\mathrm{c}}R_{tr}\right)\mathrm{sinc}[(T_r - \tau_{im})(f_r - K_r\tau_{im} + f_d)](T_r \\ - \tau_{im})\mathrm{sinc}[T_i(f_i - f_d)]T_i \end{aligned} \tag{12}$$

After range focusing, the target energy is concentrated within the sinc signal envelope.

4.1. Ideal Array Slant Range History

If the array is ideal, the apparent range of the target is:

$$R_{s0}(m,n) = R_{tr0} - \frac{f_d c}{2K_r} \approx R_{tr0} \tag{13}$$

The distance from the grid point to the array elements is calculated based on the grid position and the ideal transmit-receive positions, which can be expressed as:

$$\begin{aligned} R_g(m,n) =\ & \frac{1}{2}\left\{\begin{array}{l}\sqrt{x_{t0}^2(m) + y_{gy}^2 + \left[z_{gz} - z_{t0}(m)\right]^2} \\ +\sqrt{x_{r0}^2(n) + y_{gy}^2 + \left[z_{gz} - z_{r0}(n)\right]^2}\end{array}\right\}_{\theta_{gz}=0} \\ =\ & R_{g0} - \frac{1}{2}sin\theta_{gz}(z_{t0} + z_{r0}) \\ & + \frac{1}{4R_{g0}}\left[cos^2\theta_{gz}(z_{t0}^2 + z_{r0}^2) + (x_{t0}^2 + x_{r0}^2)\right] \\ & + \frac{1}{4R_{g0}^2}\left[sin\theta_{gz}cos^2\theta_{gz}(z_{t0}^3 + z_{r0}^3) + sin\theta_{gz}(x_{t0}^2 z_{t0} + x_{r0}^2 z_{r0})\right] \end{aligned} \tag{14}$$

It is always possible to find a point on the grid satisfying $R_{g0} = R_0$ and $\theta_{gz} = \theta_z$. If the echo is also from an ideal array, then $R_s(m,n) \approx R_g(m,n)$, and the error between them can be expressed as:

 doi:10.20944/preprints202603.2203.v1

$$\begin{aligned}\Delta R_0 &= R_g(m,n) - R_{s_0}(m,n)\\ &= \frac{1}{4R_0}[\sin^2\theta_x(x_{t0}^2 + x_{r0}^2) + 2\sin\theta_x\sin\theta_z(x_{t0}z_{t0} + x_{r0}z_{r0})]\\ &-\frac{1}{4R_0^2}\begin{bmatrix}\sin\theta_x\cos^2\theta_z(x_{t0}^3 + x_{r0}^3)\\ +(1-3\sin^2\theta_z)\sin\theta_x(x_{t0}z_{t0}^2 + x_{r0}z_{r0}^2)\\ -3\sin^2\theta_x\sin\theta_z(x_{t0}^2z_{t0} + x_{r0}^2z_{r0})\end{bmatrix}\end{aligned} \tag{15}$$

4.2. Error Array Slant Range History Error

If the array positions contain errors, the apparent range corresponding to the target is:

$$R_s(m,n) = R_{tr} - \frac{f_d c}{2K_r} \approx R_{tr} \tag{16}$$

where R_{tr} is given in Eq. (10). If the array errors are expressed as:

$$\begin{gathered}\begin{cases}x_t = x_{t0} + \Delta x_t\\ y_t = \Delta y_t\\ z_t = z_{t0} + \Delta z_t\end{cases}\quad\begin{cases}x_r = x_{r0} + \Delta x_r\\ y_r = \Delta y_r\\ z_r = z_{r0} + \Delta z_r\end{cases}\\ x_t + x_r = \Delta x_t + \Delta x_r\end{gathered} \tag{17}$$

then the error between $R_s(m,n)$ and $R_s(m,n)$ can be expressed as:

$$\begin{aligned}\Delta R &= R_g(m,n) - R_s(m,n)\\ &\approx \Delta R_0 + \frac{1}{2}\begin{bmatrix}\sin\theta_z(\Delta z_t + \Delta z_r) + \sin\theta_x(\Delta x_t + \Delta x_r)\\ +\sin\theta_y(\Delta y_t + \Delta y_r)\end{bmatrix}\\ &+\frac{1}{4R_0}\begin{bmatrix}-\cos^2\theta_x(2x_{t0}\Delta x_t + 2x_{r0}\Delta x_r)\\ +2\sin\theta_y\sin\theta_z(\Delta y_{t0}z_t + \Delta y_r z_{r0})\\ -\cos^2\theta_z(2z_{t0}\Delta z_t + 2z_{r0}\Delta z_r)\\ +2\sin\theta_x\sin\theta_y(x_{t0}\Delta y_t + x_{r0}\Delta y_{r0})\end{bmatrix}\\ &+\frac{1}{4R_0^2}\begin{Bmatrix}-\sin\theta_z\cos^2\theta_z(3z_{t0}^2\Delta z_t + 3z_{r0}^2\Delta z_r)\\ -\sin\theta_z(2x_{t0}z_{t0}\Delta x_t + 2x_{r0}z_{r0}\Delta x_r + x_{t0}^2\Delta z_t + x_{r0}^2\Delta z_r)\\ -(1-3\sin^2\theta_x)[\sin\theta_y(x_{t0}^2\Delta y_t + x_{r0}^2\Delta y_r)]\\ +6\sin\theta_x\sin\theta_y\sin\theta_z(x_{t0}\Delta y_t z_{t0} + x_{r0}\Delta y_r z_{r0})\end{Bmatrix}\end{aligned} \tag{18}$$

The additional error caused by the array position difference can be decomposed into three components can be expressed as:

$$\begin{aligned}\Delta R &= \Delta R_x + \Delta R_y + \Delta R_z\\ \Delta R_r &= \frac{1}{2}\sin\theta_x(\Delta x_t + \Delta x_r) - \frac{1}{2R_0}\cos^2\theta_x(x_{t0}\Delta x_t + x_{r0}\Delta x_r)\\ &-\frac{1}{2R_0^2}\sin\theta_z(x_{t0}z_{t0}\Delta x_t + x_{r0}z_{r0}\Delta x_r)\\ \Delta R_y &= \frac{1}{2}\sin\theta_y(\Delta y_t + \Delta y_r) + \frac{1}{2R_0}\begin{bmatrix}\sin\theta_y\sin\theta_z(\Delta y_{t0}z_{t0} + \Delta y_r z_{r0})\\ +\sin\theta_x\sin\theta_y(x_{t0}\Delta y_{t0} + x_{r0}\Delta y_{r0})\end{bmatrix}\\ &+\frac{1}{4R_0^2}\{-(1-3\sin^2\theta_x)[\sin\theta_y(x_{t0}^2\Delta y_t + x_{r0}^2\Delta y_r)]\\ &+6\sin\theta_x\sin\theta_y\sin\theta_z(x_{t0}\Delta y_t z_{t0} + x_{r0}\Delta y_r z_{r0})\}\\ \Delta R_z &= \frac{1}{2}\sin\theta_z(\Delta z_t + \Delta z_r) - \frac{1}{2R_0}\cos^2\theta_z(z_{t0}\Delta z_t + z_{r0}\Delta z_r)\\ &+\frac{1}{4R_0^2}\begin{Bmatrix}-\sin\theta_z\cos^2\theta_z(3z_{t0}^2\Delta z_t + 3z_{r0}^2\Delta z_r)\\ -\sin\theta_z(x_{t0}^2\Delta z_t + x_{r0}^2\Delta z_r)\end{Bmatrix}\end{aligned} \tag{19}$$

In this paper, $R_0 = 5$, $x_{t0}, x_{r0} \le 0.05$, $z_{t0}, z_{r0} \le 0.36$, $\theta_x, \theta_y \le 30^\circ$, and $\theta_z \approx 90^\circ$. Therefore, the above errors can be approximated as:

 doi:10.20944/preprints202603.2203.v1

$$\begin{aligned} \Delta R &= \Delta R_x + \Delta R_y + \Delta R_z \\ \Delta R_x &= \frac{1}{2}\sin\theta_x(\Delta x_t + \Delta x_r) \\ \Delta R_y &= \frac{1}{2}\sin\theta_y(\Delta y_t + \Delta y_r) \\ \Delta R_z &= \frac{1}{2}\sin\theta_z(\Delta z_t + \Delta z_r) \end{aligned} \tag{20}$$

Among these, the Y-direction error has the largest impact. The resulting phase error is:

$$\phi = \frac{4\pi}{\lambda}\sin\theta_y \Delta y \tag{21}$$

If the error takes the form of a quadratic phase error, the requirement that the phase error $\leq \pi/4$ leads to the position error requirement:

$$\Delta y \leq \frac{\lambda}{16\sin\theta_y} \approx \frac{\lambda}{16} \tag{22}$$

In this paper, the wavelength is approximately 0.0032 m = 3.2 mm, and the position accuracy requirement is 0.02 mm. If the error takes the form of a random error with standard deviation σ_y, the resulting Integrated Side-Lobe Ratio (ISLR) increment is:

$$\Delta ISLR = \left(\frac{4\pi}{\lambda}\sin\theta_y\right)^2 \sigma_y^2 \approx \left(\frac{4\pi}{\lambda}\sigma_y\right)^2 \tag{23}$$

Therefore, if the ideal ISLR = -23.6 dB and the error-induced ISLR increment ≤ 0.5 dB, the requirement is $\sigma_y \leq 0.01$ mm.

5. MIMO Radar Imaging Experimental Results and Analysis

5.1. Metal Plate Imaging Analysis

Based on the above analysis, Figure 5(a) shows the actual radar prototype. The radar prototype is used for penetration imaging experiments. The metal plate shown in Figure 5(b) is the imaging target, and the metal plate is placed inside the non-woven fabric bag shown in Figure 5(c).

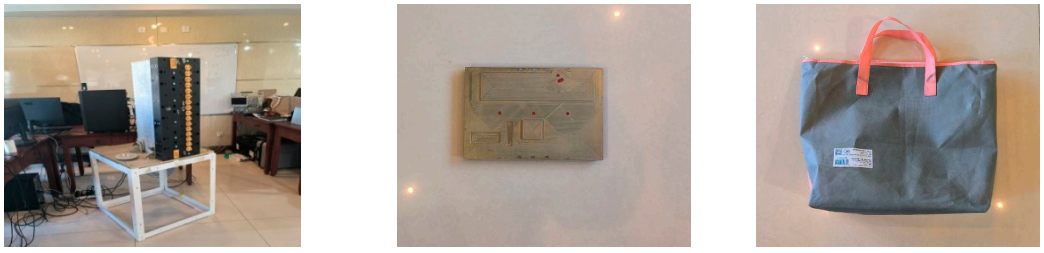

(**a**) (**b**) (**c**)

Figure 5. MIMO radar; imaging target;and obstruction. (a) MIMO radar prototype; (b) Metal plate; (c) Non-woven fabric bag.

The imaging results are shown in Figure 6. Figure 6(a) and Figure 6(b) present the conventional processing image and the range super-resolution processed image, respectively. From Figure 6(a), it can be observed that, except for the strong scattering characteristics exhibited by the bag opening zipper, the obstruction effect of the fabric bag is minimal. The outline of the internal metal plate is visible. The imaging algorithm accurately restored the spatial geometric position of the metal plate. From the range super-resolution processed imaging result in Figure 6(b), compared with Figure 6(a), the metal plate image has clearer edge contours. The left and right contours of the imaging result are sharper lines, and the edges are not blurred.

Preprints.org (www.preprints.org) | NOT PEER-REVIEWED | Posted: 27 March 2026 doi:10.20944/preprints202603.2203.v1

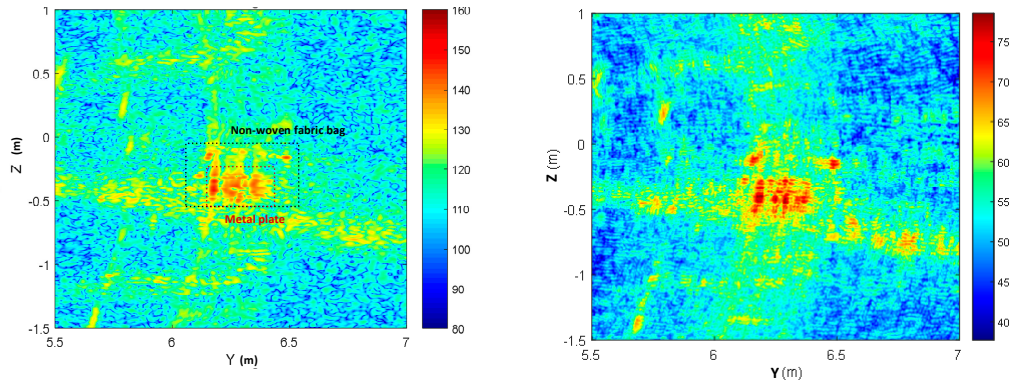

Figure 6. Metal plate imaging inside non-woven fabric. (a) Conventional processing image of the metal plate in the non-woven fabric bag; (b) Range super-resolution processed image of the metal plate in the non-woven fabric bag.

5.2. Array Error Imaging Simulation Analysis

Based on the array error theoretical analysis, imaging simulations are performed. The target parameters are: range 5 m, azimuth -0.3 m, elevation -0.3 m.

5.2.1. Elevation Error

The imaging results for different spacings are shown in Figure 7.

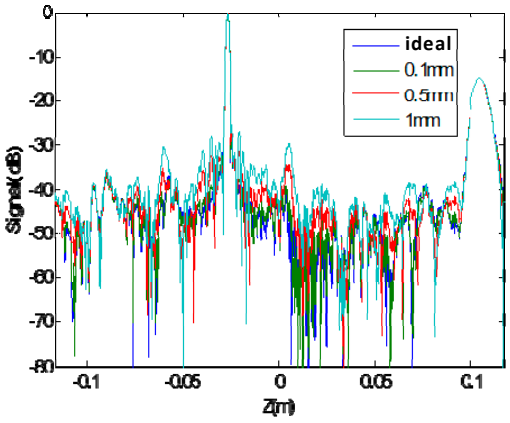

Figure 7. Elevation imaging results.

When errors exist in the elevation direction of the transmit elements, the imaging results and parameter summary are shown in Figure 7 and Table 1, respectively. The larger the elevation array position error, the greater the increments in the elevation ISLR and PSLR, and the imaging results show slight degradation compared to the ideal array imaging.

Table 1. Parameter summary.

Parameter	Value			
Tx elevation spacing (mm)	0	0.1	0.5	1
Signal amplitude (dB)	0	0	-0.030	-0.090
Range resolution (m)	1.6	1.6	1.6	1.6
Elevation resolution (m)	1.43	1.43	1.43	1.43
Elevation PSLR (dB)	-27.64	-27.43	-26.43	-25.02
Elevation ISLR (dB)	-23.63	-23.53	-21.11	-17.32

 doi:10.20944/preprints202603.2203.v1

Elevation grating lobe (dB)	-36.94	-37.63	-34.39	-29.46

5.2.2. Azimuth Error

When errors exist in the azimuth direction of the transmit elements, the imaging results and parameter summary are shown in Figure 8 and Table 2, respectively. The larger the azimuth array position error, the greater the increments in the ISLR and PSLR of the elevation imaging results, and the imaging results show slight degradation compared to the ideal array imaging. The impact on range imaging results is negligible.

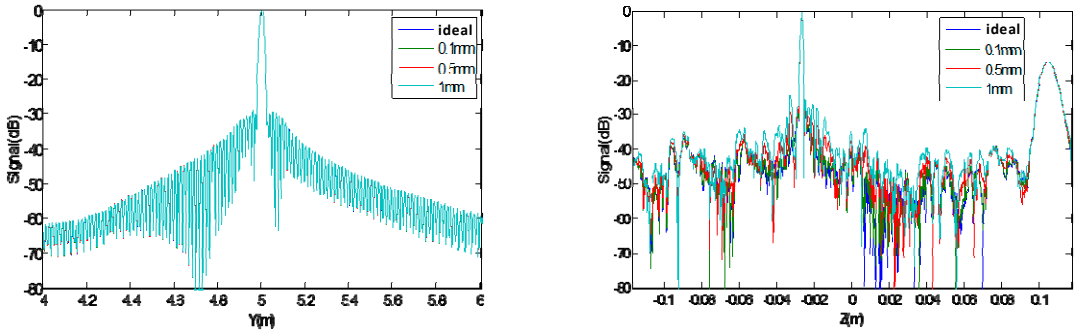

(**a**) (**b**)

Figure 8. Imaging results. (a) Range imaging results; (b) Elevation imaging results.

Table 2. Parameter summary.

Parameter	Value			
Tx azimuth spacing (mm)	0	0.1	0.5	1
Signal amplitude (dB)	0	0	-0.02	-0.08
Range resolution (m)	1.6	1.6	1.6	1.6
Elevation resolution (m)	1.43	1.43	1.44	1.43
Elevation PSLR (dB)	-27.64	-27.43	-26.48	-24.27
Elevation ISLR (dB)	-23.63	-23.46	-21.07	-17.5
Elevation grating lobe (dB)	-36.94	-36.76	-35.58	-33.63

5.2.3. Range Error

When errors exist in the range direction of the transmit elements, the imaging results and parameter summary are shown in Figure 9 and Table 3, respectively. The larger the range-direction array position error, the greater the increments in the ISLR and PSLR of the elevation imaging results. The elevation imaging results show significant degradation compared to the ideal array imaging. The impact on range imaging results is negligible.

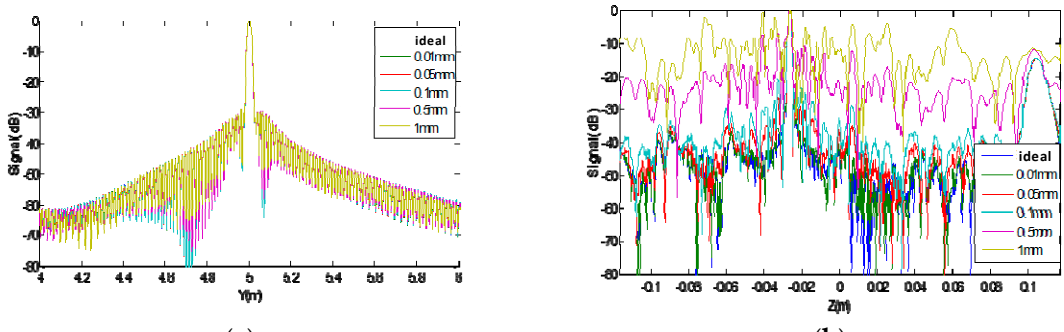

(**a**) (**b**)

Figure 9. Imaging results. (a) Range imaging results; (b) Elevation imaging results.

 doi:10.20944/preprints202603.2203.v1

Table 3. Parameter summary.

Parameter	Value					
Tx range spacing (mm)	0	0.01	0.05	0.1	0.5	1
Signal amplitude (dB)	0	0	-0.05	-0.21	-4.86	-12.82
Range resolution (m)	1.6	1.6	1.6	1.6	1.6	1.6
Elevation resolution (m)	1.43	1.43	1.43	1.43	1.54	1.56
Elevation PSLR (dB)	-27.64	-27.33	-25.86	-20.73	-6.58	-0.35
Elevation ISLR (dB)	-23.63	-23.25	-18.91	-14.27	0.22	9.16
Elevation grating lobe (dB)	-36.94	-36.59	-34.13	-28.93	-12.28	-1.95

5.2.4. Summary

Based on the above analysis, among the azimuth, elevation, and range array positions, the range-direction array position error has the most significant impact. It primarily affects the elevation imaging quality, including signal amplitude, peak sidelobe, integrated sidelobe, and main lobe width. If the constraints require negligible resolution broadening and PSLR and ISLR degradation ≤ 0.5 dB, the position accuracy must be 0.01 mm.

6. Conclusion

This paper proposes a high-resolution MIMO millimeter-wave radar imaging method for non-cooperative targets and completes experimental validation. By utilizing the large bandwidth of millimeter waves and the elevation MIMO linear array, two-dimensional range-elevation imaging of targets is achieved, effectively addressing the existing problems of traditional mechanical scanning and electronic scanning technologies. To address the issue of low target imaging resolution, range super-resolution technology is introduced to break through the physical bandwidth limitation on range resolution. The theoretical impact of array errors on imaging results is analyzed. Experiments demonstrate that the radar system possesses excellent penetration detection capability. It can meet the requirements for rapid, non-contact security screening while reducing hardware costs, providing an effective solution for next-generation public safety screening technology. Through simulation analysis, this paper verifies the impact of array position errors on imaging, including signal amplitude, peak sidelobe, integrated sidelobe, and main lobe width, providing a theoretical basis for calibration of practical systems.

Author Contributions: Conceptualization, A.J; methodology, G.J and L.G; software, G.J; writing—original draft preparation, G.J; writing—review and editing, A.J; visualization, X.G; All authors have read and agreed to the published version of the manuscript.

Funding: This work was funded by National Key R&D Program of China (2021YFA1000401)、National Natural Science Foundation of China under Grant U22B2049 and Grant U23B2012.

Data Availability Statement: The data supporting the findings of this study are not publicly available due to confidentiality restrictions.

Acknowledgments: In addition, we would like to thank the anonymous reviewers who have helped to improve the paper.

References

1. Sheen, D.M.; McMakin, D.L.; Hall, T.E. Three-Dimensional Millimeter-Wave Imaging for Concealed Weapon Detection. *IEEE Trans. Microwave Theory Techn.* **2001**, *49*, 1581–1592, doi:10.1109/22.942570.
2. Cooper, K.B.; Dengler, R.J.; Llombart, N.; Thomas, B.; Chattopadhyay, G.; Siegel, P.H. THz Imaging Radar for Standoff Personnel Screening. *IEEE Trans. Terahertz Sci. Technol.* **2011**, *1*, 169–182, doi:10.1109/TTHZ.2011.2159556.

 doi:10.20944/preprints202603.2203.v1

3. Zeng, Z.; Wu, H.; Chen, M.; Luo, S.; He, C. Concealed Hazardous Object Detection for Terahertz Images with Cross-Feature Fusion Transformer. *Optics and Lasers in Engineering* **2024**, *182*, 108454, doi:10.1016/j.optlaseng.2024.108454.
4. GUAN Jixing, ZHANG Xian, Yi Wei, et al. A MIMO Millimeter-Wave Radar for High Resolution Imaging of Non-Cooperative Target. *Modern Radar* **2025**, *47*, 10–18, doi:10.16592/j.cnki.1004-7859.20240427001.
5. FENG Hui, TU Hao, GAO Bingxi Progress on Key Technologies of Passive Millimeter Wave and Terahertz Imaging for Human Body Screening. *Laser & Infrared* **2020**, *5*, 1395–1401, doi:10.3969/j.issn.1001-5078.2020.11.018.
6. YANG Lei, SONG Hao, SHEN Ruiyang High Sparsity and Low Sidelobe Near-Field Focused Sparse Array forThree-Dimensional Imagery. *Journal of Electronics & Information Technology* **2024**, *46*, 4471–4482, doi:10.11999/JEIT231278.
7. Chen, Y.; Wu, T.; Fu, R.; Feng, X. Research on Concealed Dangerous Goods Detection Based on Active Terahertz Active Imaging. In Proceedings of the 2024 4th International Symposium on Artificial Intelligence and Intelligent Manufacturing (AIIM); IEEE: Chengdu, China, December 20 2024; pp. 808–812.
8. Zhuge, X.; Yarovoy, A.G. Sparse Multiple-Input Multiple-Output Arrays for High-Resolution near-Field Ultra-Wideband Imaging. *IET Microw. Antennas Propag.* **2011**, *5*, 1552–1562, doi:10.1049/iet-map.2010.0561.
9. Nongkseh, P.; Sur, S.N.; Kandar, D. Detection of Concealed Object Using Terahertz Images: A Comprehensive Review. *Engineering Applications of Artificial Intelligence* **2025**, *148*, 110432, doi:10.1016/j.engappai.2025.110432.
10. Zhuge, X.; Yarovoy, A.G. A Sparse Aperture MIMO-SAR-Based UWB Imaging System for Concealed Weapon Detection. *IEEE Trans. Geosci. Remote Sensing* **2011**, *49*, 509–518, doi:10.1109/TGRS.2010.2053038.
11. Gao, J.; Qin, Y.; Deng, B.; Wang, H.; Li, X. Novel Efficient 3D Short-Range Imaging Algorithms for a Scanning 1D-MIMO Array. *IEEE Trans. on Image Process.* **2018**, *27*, 3631–3643, doi:10.1109/TIP.2018.2821925.
12. Gumbmann, F.; Schmidt, L.-P. Millimeter-Wave Imaging With Optimized Sparse Periodic Array for Short-Range Applications. *IEEE Trans. Geosci. Remote Sensing* **2011**, *49*, 3629–3638, doi:10.1109/TGRS.2011.2164616.
13. Ahmed, S.S.; Schiessl, A.; Schmidt, L.-P. A Novel Fully Electronic Active Real-Time Imager Based on a Planar Multistatic Sparse Array. *IEEE Trans. Microwave Theory Techn.* **2011**, *59*, 3567–3576, doi:10.1109/TMTT.2011.2172812.
14. Linder, M.; Schmidt, D.; Schwarz, D.; Riese, N.; Waldschmidt, C. A Sub-Aperture-Based Calibration Algorithm for MIMO Antenna Arrays. *IEEE Open J. Antennas Propag.* **2025**, *6*, 548–559, doi:10.1109/OJAP.2025.3537681.
15. Kwon, Y.; Seo, K.; Kim, C.K. Enhancing Calibration Precision in MIMO Radar with Initial Parameter Optimization. *Remote Sensing* **2025**, *17*, 389, doi:10.3390/rs17030389.
16. LIANG Mengwei, HE Jin, SHU Ting, YU Wenxian Linear Coprime Sensor Location Arrays: Array Calibration and Beamforming. *Journal of Electronics & Information Technology* **2024**, *46*, 240–248, doi:10.11999/JEIT221539.
17. Zhu, R.; Zhou, J.; Chen, S.; Ding, H. Pseudo-Trapezoidal Fast Factorized Backprojection Algorithm for Near-Field Sparse MIMO Array 3-D Imaging. *IEEE Trans. Aerosp. Electron. Syst.* **2025**, 1–16, doi:10.1109/TAES.2025.3580015.
18. Ivanenko, Y.; Batra, A.; Vu, V.T.; Pettersson, M.I.; Kaiser, T. Experimental Results of Local Backprojection for Monostatic THz SAR Imaging. In Proceedings of the 2025 International Conference on Mobile and Miniaturized Terahertz Systems (ICMMTS); IEEE: Dubai, United Arab Emirates, February 23 2025; pp. 1–5.
19. Focsa, A.; Anghel, A.; Datcu, M. Accelerated Back-Projection SAR Processor on Arbitrary Elliptical Imaging Grid With Azimuth Spectrum Unfolding. *IEEE Geosci. Remote Sensing Lett.* **2023**, *20*, 1–5, doi:10.1109/LGRS.2023.3298696.
20. WANG Huaijun, HUANG Chunlin, LU Min Back Projection Imaging Algorithm for MIMO Radar. *Systems Engineering and Electronics* **2010**, *32*, 1567–1572, doi:10.3969/j.issn.1001-506X.2010.08.03.
21. Roberts, W.; Stoica, P.; Li, J.; Yardibi, T.; Sadjadi, F.A. Iterative Adaptive Approaches to MIMO Radar Imaging. *IEEE J. Sel. Top. Signal Process.* **2010**, *4*, 5–20, doi:10.1109/JSTSP.2009.2038964.

 doi:10.20944/preprints202603.2203.v1

22. Oral, O.; Oktem, F.S. Plug-and-Play Regularization on Magnitude With Deep Priors for 3D Near-Field MIMO Imaging. *IEEE Trans. Comput. Imaging* **2024**, *10*, 762–773, doi:10.1109/TCI.2024.3396388.
23. Gumbmann, F.; Schmidt, L.-P. Design of Sparse MIMO Arrays for Short Range Imaging Applications. *Proc. Asia-Pacific Microwave Conference* **2010**, 1653–1656.